Energy Storage Materials 17 (2019) 1–11

Contents lists available at ScienceDirect

Energy Storage Materials

journal homepage: www.elsevier.com/locate/ensm

Free-standing SnS/C nanofiber anodes for ultralong cycle-life lithium-ion batteries and sodium-ion batteries

Jing Xia[a], Li Liu[a,b,*], Sidra Jamil[a], Jianjun Xie[a], Hanxiao Yan[a], Yiting Yuan[a], Yue Zhang[a], Su Nie[a], Jing Pan[a], Xianyou Wang[a], Guozhong Cao[c,**]

[a] National Base for International Science & Technology Cooperation, National Local Joint Engineering Laboratory for Key Materials of New Energy Storage Battery, Hunan Province Key Laboratory of Electrochemical Energy Storage and Conversion, School of Chemistry, Xiangtan University, Xiangtan 411105, China

[b] Key Laboratory of Advanced Energy Materials Chemistry (Ministry of Education), Nankai University, Tianjin 300071, China

[c] Department of Materials Science and Engineering, University of Washington, Seattle, WA 98195-2120, United States

ARTICLE INFO

Keywords:
Electrospinning
Free-standing, stannous sulfide
Lithium-ion batteries
Sodium-ion batteries
Anode materials

ABSTRACT

The development of flexible energy storage devices is the key to widen the application of flexible electronics and wearable devices. Flexible electrodes with superior electrochemical performance are critical components for flexible energy storage devices. Herein, we propose a simple and versatile electrospinning strategy to prepare the SnS/C nanofibers (SnS/C NFs) film. By using SnS/C NFs film directly as a free-standing anode in both lithium-ion batteries (LIBs) and sodium-ion batteries (SIBs), it can provide outstanding electrochemical performance. For LIBs, it delivers high capacities of 648 and 548 mA h g^{-1} at 200 and 500 mA g^{-1} respectively after 500 cycles. It even shows outstanding cyclability for 1000 cycles. For SIBs, it retains capacity of 481 mA h g^{-1} after 100 cycles at 50 mA g^{-1}. Moreover, the capacity remains as high as 349 mA h g^{-1} at 200 mA g^{-1} after 500 cycles. The outstanding electrochemical performance is mainly attributed to the fact that the fine SnS nanoparticles dispersed in one-dimensional porous nanofibers with uniform diameters around 130 nm shorten the transport path of ions and electrons, and the presence of N-doped carbon enhanced the electrical conductivity as well as relieve the volume change caused by the alloying/de-alloying reaction. Besides, the ultra-robust mechanical flexibility of SnS/C NFs film makes it a promising anode candidate for flexible LIB and SIB in future.

1. Introduction

Global energy shortage and environmental pollution are two main critical challenges in 21st century which are facing by mankind [1,2], so energy conversion and storage are becoming more and more important. Lithium-ion batteries (LIBs) and sodium-ion batteries (SIBs) play a key role in developing high-efficient energy storage devices. In order to fulfill the continuous requirements of long lifespan, high energy/power density and safety, the designing of adequate anode material for LIBs and SIBs is an attractive as well as extended research area among researchers. Especially, most of anode materials which are suitable for LIBs could not be used directly in SIBs [3]. Thus, the exploitation of excellent anode materials with high specific capacity and long cycle life is crucially demanded.

During the past few years, metal sulfides as anode materials is an increasing research interest for superior LIBs and SIBs owing to their high theoretical specific capacities [4–12]. Among all metal sulfides, Stannous sulfide (SnS) is highlighted by its unique layered structure and large interlayer spacing(4.04 Å for SnS vs. 0.76 Å for Li^+ and 1.02 Å for Na^+), which provides a fast channel for the transfer of ions and electrons [9]. Unfortunately, low intrinsic electronic conductivity and fatal volume change of alloying/de-alloying reaction result in large polarizations and poor electrochemical performance for bare SnS. In order to overcome these fatal factors, mixing carbon matrix with SnS is a common strategy [13–17]. For example, Youn et al. reported a SnS/N-doped reduced grapheme oxide composites which achieved a discharge capacity of 229 mA h g^{-1} after 200 cycles at a cycling rate of 200 mA g^{-1} in LIBs [15]. The SnS-C nanocomposite prepared by Wu et al. via a high-energy mechanical milling method exhibited a high capacity retention of 97.8% over 80 cycles at a current density of 100 mA g^{-1} when evaluated as anode materials in SIBs [16]. However, few SnS-based anode materials could have a ultralong cycle life span

* Corresponding author at: National Base for International Science & Technology Cooperation, National Local Joint Engineering Laboratory for Key Materials of New Energy Storage Battery, School of Chemistry, Xiangtan University, Xiangtan 411105, China.

** Corresponding author at: Department of Materials Science and Engineering, University of Washington, Seattle, WA 98195-2120, United States.

E-mail addresses: liulili1203@126.com (L. Liu), gzcao@u.washington.edu (G. Cao).

https://doi.org/10.1016/j.ensm.2018.08.005
Received 10 May 2018; Received in revised form 31 July 2018; Accepted 6 August 2018
Available online 14 August 2018
2405-8297/ © 2018 Elsevier B.V. All rights reserved.

above 500 cycles, which maybe owing to the potential for carbon hasn't been fully excavated.

Recently, under the trend of pursuing fashionable and convenient lifestyle, flexible electronics and wearable devices showed that there is an enormous increase in demand. However, conventional electrodes prepared by coating slurry on metal current collector cannot satisfy the fashionable needs for flexible electronics due to their inherently inflexible electrode structures. Free-standing electrodes are the key to realize flexible electronics and wearable devices application. Electrospinning technology is a simple and versatile strategy used in producing flexible film-based electrospun nanofibers with unique features, including certain degree of mechanical deformation (folding or flectional), controllable fiber diameters and designable morphologies (dense, hollow and porous) [18–21].

Herein, the free-standing and flexible SnS/C nanofibers (SnS/C NFs) were firstly developed via electrospinning followed by calcination. The SnS/C NFs film is directly used as a free-standing electrode in LIBs and SIBs without using conductive additive, binder and metal current collector, which show ultralong cycle life and high capacity at the same time. The facile preparation process, robust mechanical properties, and excellent electrochemical performance of the SnS/C NFs film ensure it as a promising anode candidate for flexible LIBs and SIBs.

2. Experimental section

2.1. Materials preparation

All the reagents including tin(II) chloride dihydrate ($SnCl_2{\cdot}2H_2O$, Aladdin, China), N, N-Dimethylformamide (DMF, C_3H_7NO, Sinopharm Chemical Reagent Co, Ltd, China), polyvinylpyrrolidone (PVP, $(C_6H_9NO)_n$, MW = 1,300,000, Alfa Aesar), and thiourea (CN_2H_4S, Aladdin, China) were analytically pure grade and used directly.

The schematic of the fabrication process of the SnS/C nanofibers is shown in Fig. 1. In a typical synthesis of electrospinning, 4 mmol $SnCl_2{\cdot}2H_2O$ was first dissolved into 5 mL DMF under vigorous stirring at room temperature until a clear transparent solution was obtained then 0.5 g PVP was added to the above-solution and c continuously stirred for 3 h. The obtained mixture was used as the working solution for electrospinning. The precursor solution was loaded into a 5 mL plastic syringe equipped with a flat-needle, which was connected to a single channel syringe pump. The flow rate of solution was set to be constant at 0.3 mL h^{-1}. An aluminum foil was used to collect the nanofibers, and the distance between the aluminum foil and the needle was kept at around 15 cm, and a voltage of 18 kV was applied between the needle and the grounded plate to initiate the electrospinning.

The as-collected $SnCl_2$/PVP precursor fibers were dried at 80 °C in vacuum for 6 h then the fibers were heat-treated in a muffle furnace at 2 °C min^{-1} up to 280 °C for 2 h to stabilize the fiber structure. Subsequently, the fibers were placed in a tube furnace at 250 °C for 2 h under Ar/H_2 atmosphere with a heating rate of 2 °C min^{-1} (a certain amount of thiourea be placed in the upstream of Ar/H_2 atmosphere, the weight ratio of thiourea and fibers is 5:1 (the schematic of sulfidation process is shown in Fig. S1)), after completion of the sulfidation, the nanofibers were naturally cooled to room temperature. The main gaseous products of thiourea decomposition in inert atmospheres between 182 and 330 °C are carbon disulfide (CS_2) and ammonia (NH_3) [22]. CS_2 can generate hydrogen sulfide (H_2S) and carbon (C) by hydrogenolysis reaction with H_2 in Ar/H_2 atmosphere ($CS_2 + H_2 \rightarrow H_2S + C$). H_2S is a commonly used vulcanizing agent. However, direct use of H_2S gas as a vulcanizing agent will cause serious environmental pollution and is unsafe. Therefore, using thiourea as a vulcanizing agent is more environmental friendly and safe method. Finally, remove the porcelain boat containing thiourea residue, the fibers were further carbonized in Ar/H_2 atmosphere at 650 °C for 8 h at 2 °C min^{-1}. After the glass tube naturally cooled down to room temperature, the SnS/C NFs electrode material was obtained. Besides, different carbonization temperatures (550 and 750 °C) were also attempted to prepare the SnS/C nanofibers for comparisons.

2.2. Structure and morphology characterization

X-ray diffraction (XRD, Rigaku, Ultima IV with D/teX Ultra with Cu-Kα radiation) was employed to characterize the crystalline structures of samples with a scanning rate of 5 ° min^{-1}. The carbon content and sulphur content in the SnS/C nanofibers was measured by using Elemental analyzer (Vario EL III, Elemental Analysis System GmbH, Germany). Raman spectra of the samples were characterized by a confocal Raman microspectrometer (Renishaw InVia, Derbyshire, England) with 532 nm laser source. To investigate the surface elemental states of samples, X-ray photoelectron spectra (XPS, Kratos Axis Ultra DLD, Japan) were carried

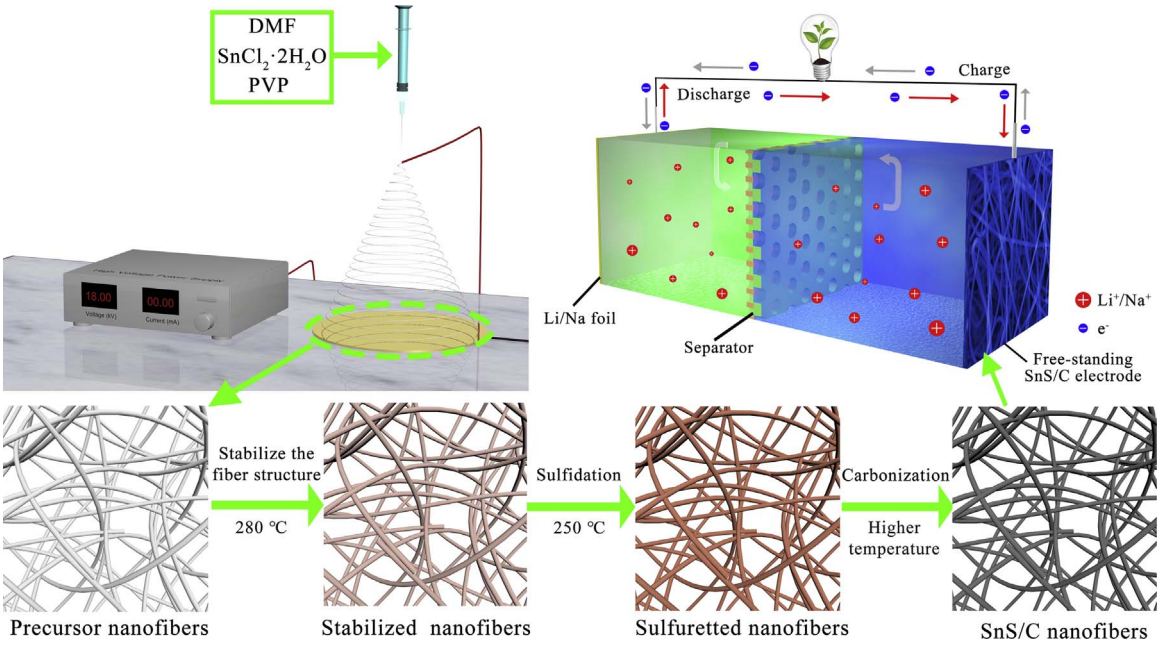

Fig. 1. Schematic illustration of the synthesis process for the SnS/C nanofibers.

out using a Kratos Axis Ultra DLD spectrometer with a monochromated Al Kα X-ray source (hν = 1486.6 eV). The morphology and microstructure were observed by field emission scanning electron microscope (FE-SEM, Carl Zeiss, SIGMA, HD-01-61, Germany) and transmission electron microscopy (TEM, FEI-Tecnai G2 TF20, America). The high-angle annular dark-field (HAADF) and corresponding STEM elemental mappings were performed using a Cs-corrected Titan G2 60–300 TEM. BET surface area of samples was calculated by the USA Micromeritics Instrument Corporation TriStar II 3020. The conductivity of the SnS/C films with different carbonization temperatures were tested by using the High Precision Resistivity Tester (YAOS, DX200GH, China).

2.3. Electrochemical tests

The free-standing SnS/C nanofiber films were directly used as electrodes without any binders, conductive additives and metal current collectors. The electrochemical performance of the electrodes was assessed using CR2025 coin cells with lithium or sodium metal as the counter/reference electrode, and the SnS/C nanofiber films were punched into disks with diameter of 1 cm as the working electrode. For LIBs, the electrolyte was composed of 1 mol L^{-1} $LiPF_6$ in a mixture of dimethyl carbonate (DMC)/ethylene carbonate (EC) with 1:1 volumetric ratio, and the celgard 2300 microporous membrane as separator. For SIBs, the electrolyte was employed with 1 mol L^{-1} $NaClO_4$ in a mixture of ethylene carbonate (EC)/propylene carbonate (PC) (1:1 vol %) with 5% fluorinated ethylene carbonate (FEC) as additive, and the glass fiber film (Whatman GF/D) as separator. All coin cells were assembled in argon-filled glove box, where both H_2O and O_2 values were kept below 1 ppm. The galvanostatic discharge/charge tests were performed by a BT3008W battery test system (Neware, Shenzhen, China). Cyclic voltammetry (CV) and electrochemical impedance spectroscopy (EIS) tests were carried out by CHI604E electrochemical workstation (Chenhua, Shanghai, China). The EIS tests were implemented a sine wave with an AC amplitude of 5 mV in 0.01 Hz to 100 kHz. Every lithium/sodium cell was activated for 1 cycle at 50 mA g^{-1} before the EIS test.

3. Results and discussion

3.1. Characterization of SnS/C NFs

The XRD patterns of SnS/C NFs obtained at different carbonation temperatures (550 °C, 650 °C and 750 °C) are shown in Fig. 2a. All XRD patterns can be well indexed to the orthorhombic SnS with Pbnm space group (JCPDS Card No. 39-0354). The main diffraction peaks located at 22.0°, 26.0°, 27.5°, 30.5°, 32.0° and 39.0° can be assigned to the (110), (120), (021), (101), (111), (040) and (131) planes, respectively. There are no detectable impurity peaks, suggesting that the orthorhombic SnS with high purity could be obtained at the carbonation temperatures above 550 °C. The orthorhombic SnS is considered to be a small distortion of the NaCl structure [23], resulting in a significant decrease in the bond strength along one axis and the semi-layered nature with a layer spacing of 4.04 Å (Fig. S2 a shows the structural model of the SnS (110) plane with the layer spacing of 4.04 Å). The large layer spacing is capable of hosting Li^+/Na^+ and provides a fast pathway for the transfer of ions and electrons. Interestingly, the (040) peak is abnormally strong in the SnS/C NFs-750 °C. Fig. S2c and d show the structural models of the (040) and (111) plane of orthorhombic SnS, respectively. According to previous research [24], the surface energies (σ) of some lattice planes of orthorhombic SnS increases in the sequence: σ (100) < σ (001) < σ (010) < σ (111). At lower temperatures (550 °C and 650 °C), owing to the low surface energy of (100) and (001) planes, SnS crystals preferentially grow along (111) planes with (100) and (001) planes as base planes. When the temperature is raised to 750 °C, SnS crystals preferentially grow along high-index (040) planes and have (010) as base planes. Reddy [24] and Nwofe et al. [25] also observed similar preferential growth of the (040) plane with increasing temperature. The Raman spectrum of SnS/C NFs with different carbonation temperatures are shown in Fig. 2b. Two Raman shift peaks located at around 1360 cm^{-1} and 1580 cm^{-1}, which are attributed to the D-bands (disordered structure) and G-bands (graphitic structure) of carbon materials, respectively [26]. The results of XRD and Raman demonstrate that the sample obtained is a composite of SnS and C.

The carbon content , the nitrogen contents and the sulphur content of samples were determined by elemental analyzer and the results are shown in Table S1. The carbon content in SnS/C NFs-550 °C, SnS/C NFs-650 °C and SnS/C NFs-750 °C are estimated to be 25.3 wt%, 25.6 wt% and 45.7 wt%, respectively. Besides, the SnS content is also calculated based on the measured sulfur content, the value of SnS/C NFs-550 °C, SnS/C NFs-650 °C and SnS/C NFs-750 °C are 68.8 wt%, 69.7 wt% and 49.4 wt%. It is worth noting that the SnS content decreased significantly when the carbonation temperature reached to 750 °C. Refer to related literature [27], owing to the lower melting point of SnS, which partially evaporates, finally leading to the loss of SnS. Because of the presence of N–C bonds in PVP, a small amount of self-doped nitrogen is also detected in these three samples. The total contents of SnS, carbon and nitrogen for the SnS/C NFs-650 °C and the SnS/C NFs-750 °C are close to 100 wt%. However, the total contents of SnS, carbon and nitrogen for the SnS/C NFs-550 °C are only 98.6 wt%, which mainly be attributed to some PVP are not completely carbonized.

From the XPS full spectrum of SnS/C NFs-650 °C (Fig. 3a), O, Sn, N, C, and S elements were identified. Fig. 3b shows the high-resolution S2p spectrum of SnS/C NFs-650 °C. The peak at 161.9 eV can be assigned to

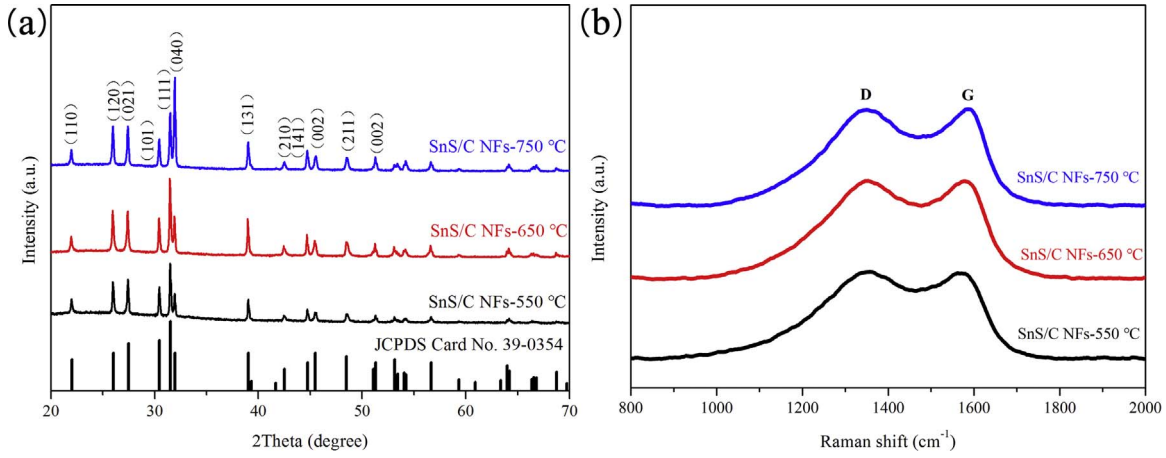

Fig. 2. XRD patterns (a) and Raman spectrums (b) of SnS/C NFs with different carbonation temperatures.

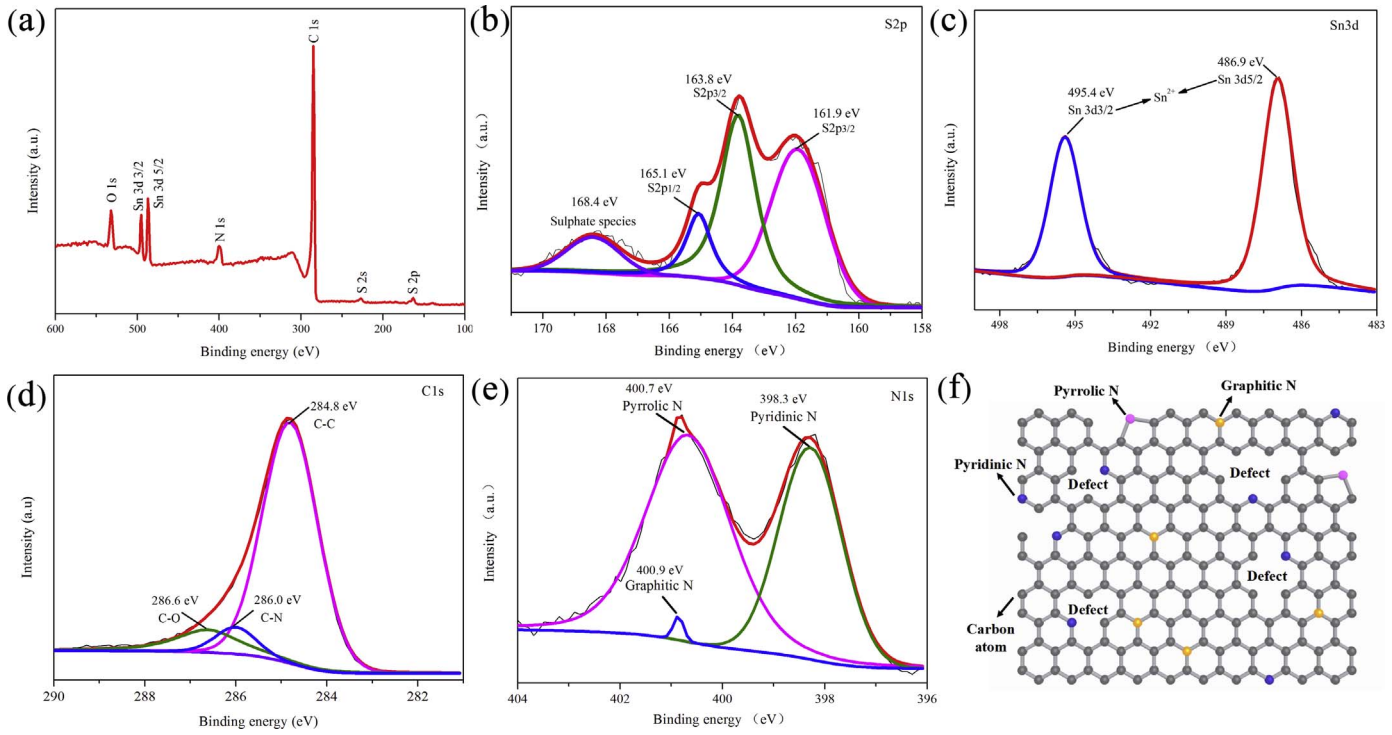

Fig. 3. XPS full spectrum (a) of the SnS/C NFs-650 °C. XPS high-resolution spectrum of S2p (b), Sn3d (c), C1s (d) and N1s (e) for the SnS/C NFs-650 °C. (f) Schematic structure of the graphitic N, pyrrolic N and pyridinic N in SnS/C NFs-650 °C.

S2p3/2 of S^{2-} in SnS [28]. There are another two peaks at 165.1 and 163.8 eV are in accordance with the C-S-C heterocyclic configuration [29], and the weak peak at 168.4 eV is generally accepted as the sulphate species (contain C-SO_x-C (x = 2–4) groups) [30–32]. These C–S–C bonds are surrounded by abundant electrons, which enhance the electrochemical reaction kinetics of SnS. Furthermore, the C–S–C covalent bonds may play an important role in stabilizing the structure of SnS. The chemical state of Sn is also depicted by the Sn3d high-resolution spectrum in Fig. 3c, the two peaks situated at 495.4 eV and 486.9 eV can be attributed to Sn3d3/2 and Sn3d5/2 of Sn^{2+} in SnS, respectively [33,34]. As shown in Fig. 3d, the high-resolution spectrum of C1s can be decomposed into three species. The dominated peak located at 284.8 eV is ascribed to the C–C bond, and two minor peaks located at 286.6 eV and 286.0 eV, suggested the presence of C–O bond and C–N bond, respectively [35–37]. Besides, the high-resolution N1s spectrum (Fig. 3e) verifies that the presence of graphitic N (400.9 eV), pyrrolic N (400.7 eV) and pyridinic N (398.3 eV) [38,39]. Fig. 3f illustrates the three types of N structure. These self-doped N contributed a large number of electrons for the π-conjugated system of carbon [40], which definitely improves the electronic conductivity of SnS/C NFs. Furthermore, the pyrrolic N and pyridinic N can induce some defects in carbon and provide some active sites for Li^+/Na^+ storage [41].

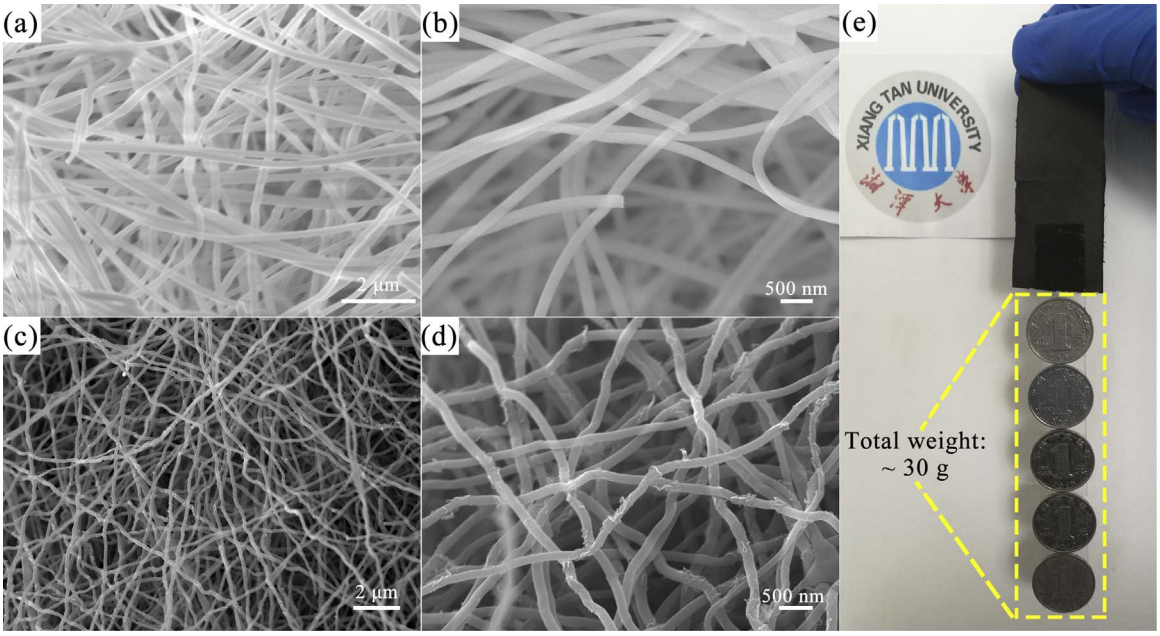

Fig. 4. FE-SEM images of as-spun $SnCl_2$/PVP nanofibers (a, b) and the SnS/C NFs-650 °C (c, d). (e) Several Chinese coins (the weight of each 1 yuan coin is about 6 g) taped to edge of SnS/C NFs-650 °C.

Fig. 4 reveals the field emission scanning electron microscope (FE-SEM) images for the as-spun (Fig. 4a, b) and carbonized fibers (Fig. 4c, d). The as-spun $SnCl_2$/PVP fibers are long and smooth with uniform diameters around 200 nm. Compared to the as-spun fibers, the diameter of the carbonized fibers is shrunk to around 130 nm, but their fibrous morphology is perfectly maintained. These obtained fine nanofibers are closely woven into interconnecting network, which not only facilitated both fast ionic and electronic transport, but also enhanced the anti-strain ability. The mechanical flexibility of obtained carbonized fibers is intuitively expressed by Fig. 4e. The SnS/C NFs film can endure the weight of five 1 yuan Chinese coins (the weight of each 1 yuan Chinese coin is about 6 g) without any breakage. For further evaluating the mechanical robustness of SnS/C NFs films, a video is appended to the Supplementary Video 1 (some video screenshots show in Fig. S3). From the video, the SnS/C NFs films are intact after being folded, bent and kneaded. This ultra-robust mechanical flexibility benefits primarily from the support of interconnecting carbon fiber networks, which provides a prerequisite for excellent electrochemical performance. In addition, BET surface area and pore size distribution of samples are displayed in Fig. S4. The specific surface area of SnS/C NFs-550 °C , SnS/C NFs-650 °C and SnS/C NFs-750 °C is as high as 102, 109 and 138 $m^2 g^{-1}$ respectively and their pore volume successively is 0.069, 0.077 and 0.104 $cm^3 g^{-1}$. The apparently increased specific surface area and pore volume of SnS/C NFs-750 °C is mainly attributable to the evaporation of some SnS resulting in the formation of more voids. For the pore size distribution of samples, the pore diameter of three samples mainly converges within the range of 1.5 to 2.5 nm. The large specific surface areas and fine porous structure not only accelerate the transfer of ions and electrons, but also buffering the volume change in discharge-charge process, thereby further enhancing electrochemical performance of the composite.

Supplementary material related to this article can be found online at doi:10.1016/j.ensm.2018.08.005.

To understand the distribution of SnS in carbon fiber, transmission electron microscopy (TEM) analysis is performed. The TEM images (Fig. 5a) show that uniform fibrous morphology with a diameter of around 130 nm. As revealed by the EDX element mapping (inset in Fig. 5b), the element of C, N, S and Sn were uniformly distributed in the fibers. The high resolution TEM (HRTEM) images (Fig. 5c) and interplanar crystal spacing statistical tables (inset in Fig. 4c) reveals the clear lattice fringes with a space of 3.42 Å and 1.87 Å corresponding to the (120) and the (211) planes of the orthorhombic SnS (Pbnm space group), which match with the XRD results (Fig. 2a). To ascertain the size of SnS particles, the Cs-corrected HAADF images and corresponding STEM elemental mappings were obtained by a Cs-corrected TEM. As shown in Fig. S5, SnS exhibits an extremely small particle size of 1–3 nm. These fine nanoparticles are dispersed in the carbon nanofibers which can better relieve the volume change caused by the alloying/de-alloying reaction, which ensured high-efficiency utilization for the carbon matrix. The STEM elemental mappings also further verified that the element of C, N, S and Sn were uniformly distributed in the fibers.

Further, the SnS/C NFs-650 °C were heat-treated in a muffle furnace at 1 °C min^{-1} up to 700 °C for 4 h to remove the carbon matrix. The obtained samples were identified by XRD, XRD pattern (Fig. S6a) suggests that all the diffraction peaks can be assigned to the tetragonal SnO_2 (JCPDS Card No. 41-1445). In addition, we provide the digital image of SnO_2 nanofiber film in Fig. S6b. It can be observed from the figure, there are many cracks on the surface of the SnO_2 nanofiber film. This nanofiber film becomes fragile and loses mechanical flexibility due to the absence of carbon skeletons. Fig. S6 (c, d) show the FE-SEM images of SnO_2, it can be seen that most of the nanofibers have been broken into shorter fibers and the diameter of the fibers is not uniform from 40 to 60 nm. Besides, some non-fibrous clumps are found in the marked yellow elliptical area, which was attributed to the shedding of nanoparticles that were agglomerated into clumps. The TEM images in Fig. 5d and e also show that the sample still maintains the fibrous morphology composed of SnO_2 nanoparticles but non-uniform diameter. The inset in Fig. 5e displays the EDX elemental mapping for O and Sn. From the EDX element mapping, O and Sn were uniformly distributed in the nanofibers. In the HRTEM image (Fig. 5f) and interplanar crystal spacing statistical tables (inset in Fig. 5f), the lattice

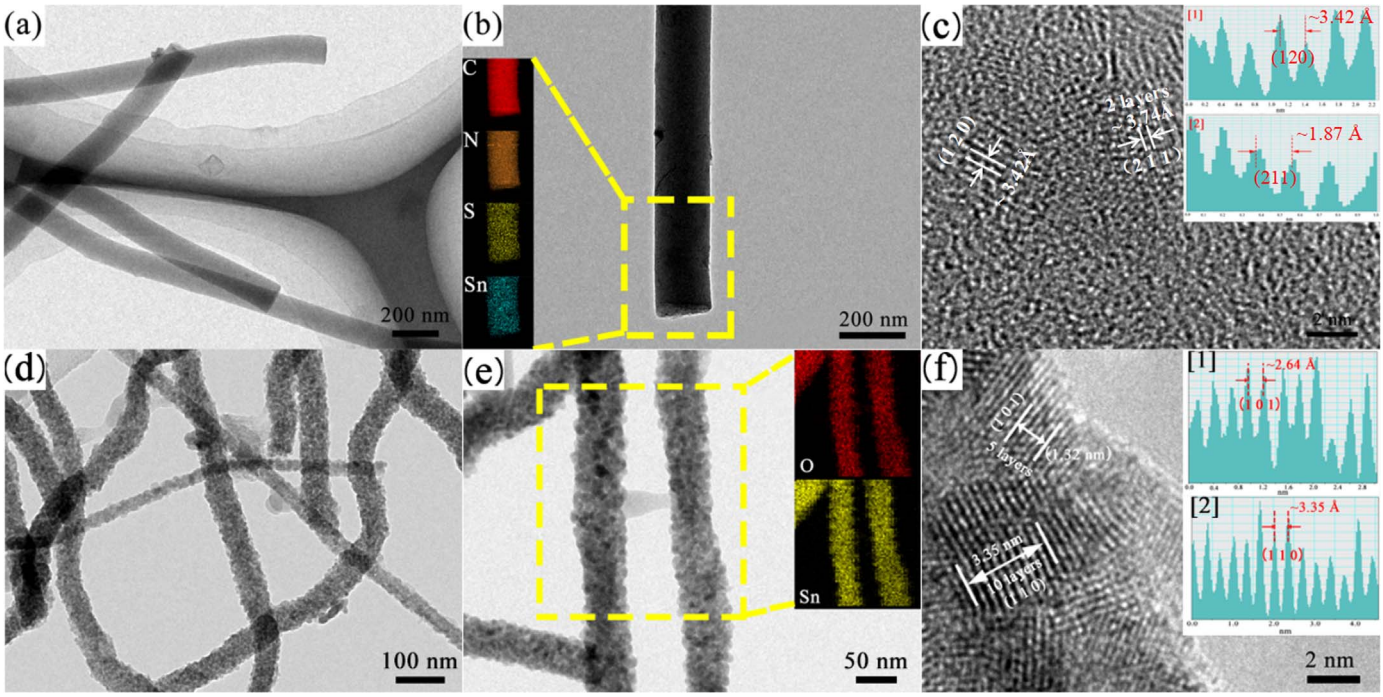

Fig. 5. (a, b) TEM images of SnS/C NFs-650 °C (the EDX elemental mapping of the area, marked by the yellow rectangle in image b). (c) HR-TEM image and interplanar crystal spacing statistical tables (the inset) of SnS/C NFs-650 °C. (d, e) TEM images of SnO_2 nanofibers (the EDX elemental mapping of the area, marked by the yellow rectangle in image (e)). (f) HR-TEM image and interplanar crystal spacing statistical tables (inset in (f)) of SnO_2 nanofibers. (For interpretation of the references to color in this figure legend, the reader is referred to the web version of this article.)

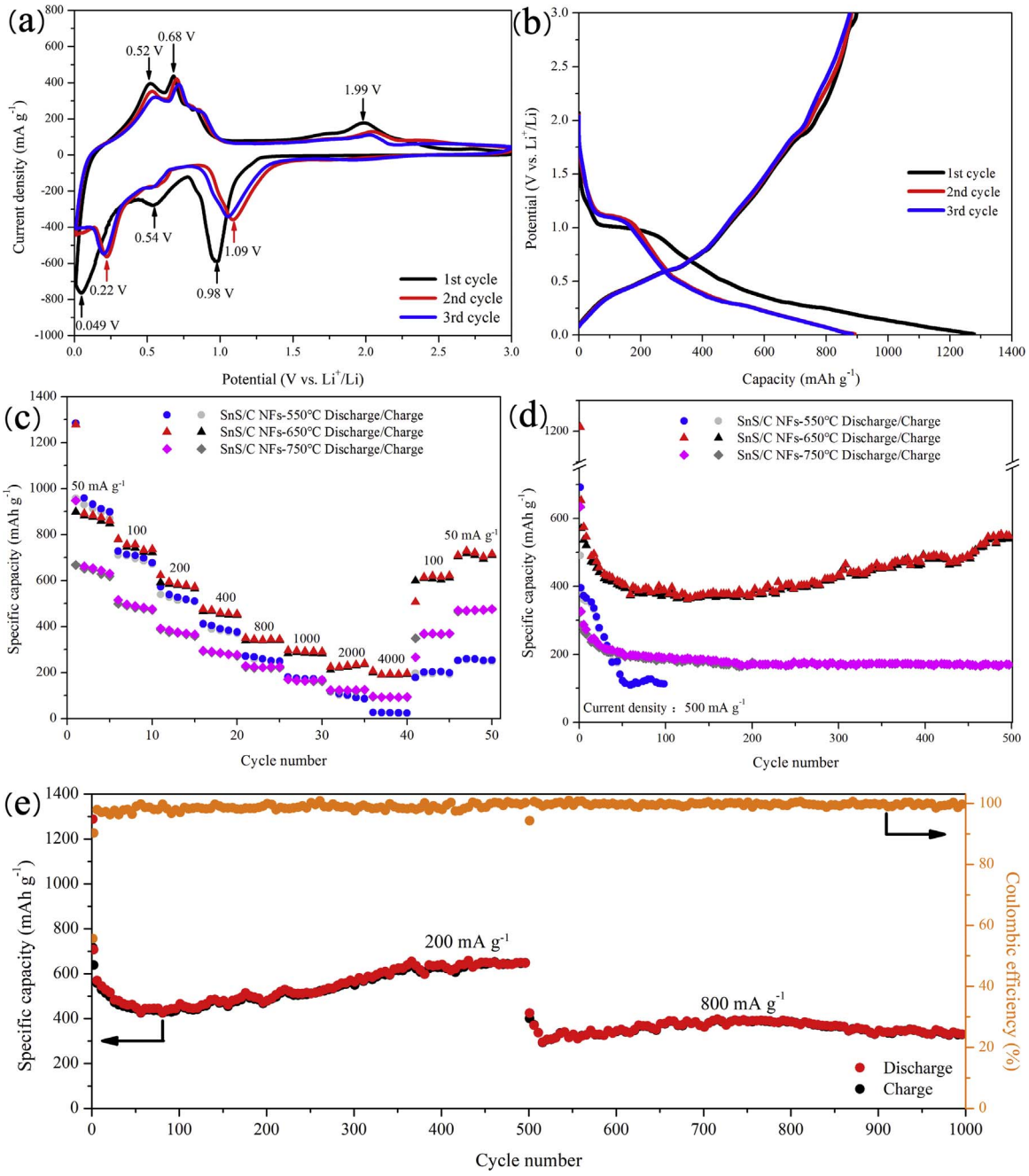

Fig. 6. (a) Cyclic voltammetry curves of SnS/C NFs-650 °C between 0.01 and 30 V with a scan rate of 0.1 mV s^{-1}. (b) Discharge-charge voltage profiles of SnS/C NFs-650 °C at a rate of 50 mA g^{-1}. (c) Rate performance of SnS/C NFs with different carbonization temperatures at various current densities from 50 mA g^{-1} to 4000 mA g^{-1}. (d) Cycling performance of SnS/C NFs with different carbonization temperatures at a current density of 500 mA g^{-1}. (e) Long-term cycling performance for SnS/C NFs-650 °C.

fringes with a space of 2.64 Å and 3.35 Å corresponding to (101) and (110) plane of SnO_2 can be identified, which also match with the XRD result of SnO_2 (Fig. S6a).

3.2. Electrochemical evaluation in LIBs

Fig. 6a shows the first three cycle's cyclic voltammetry (CV) for the SnS/C NFs-650 °C electrode at the potential window of 0.01 to 3.0 V (vs. Li^+/Li) with the san rate of 0.1 mV s^{-1}. In the first cathodic sweep, the reduction peak at 0.98 V could be assigned to the conversion reaction of SnS ($SnS + 2Li^+ + 2e^- \rightarrow Sn + Li_2S$) [4]. The distinctive reduction peak at 0.54 V could be attributed to the irreversible formation of solid electrolyte interface (SEI) films, which can lead to large irreversible capacity loss in the first cycle. The peak at below 0.30 V may contain the alloying reaction process ($Sn + xLi^+ + xe^- \leftrightarrow Li_xSn$ ($0 < x \leq 4.4$)) [42]. For the anodic sweep, the de-alloying reactions separated into two individual peaks at 0.52 V and 0.68 V, showing the multi-step de-alloying process which is similar to previous literatures [43–45]. The oxidation/reduction peaks located at 1.99 V/1.09 V probably originated from the reversible conversion reaction of SnS. Fig. 6b shows that the first three discharge-charge curves of the SnS/C NFs-650 °C electrode at 50 mA g^{-1}. All the capacities in present work were calculated based on the full mass of SnS/C composite. The first discharge and charge capacities can reach 1278 mA h g^{-1} and 898 mA h g^{-1}, respectively. The initial coulombic efficiency is approximate 70.3%, the capacity loss of 29.7% is mainly ascribe the electrolyte decomposition and the inevitable formation of SEI films. At subsequent cycles, almost overlapping discharge curves are obtained, demonstrating the

minimized polarization for SnS/C NFs electrode.

The electrochemical performance of the SnS/C NFs electrode was evaluated by the discharge-charge test of the galvanostatic condition. Fig. 6c compared the rate performance of the SnS/C NFs with different carbonization temperatures at various current densities. Obviously, the SnS/C NFs electrode with carbonization temperatures of 650 °C shows best rate performance compared with other two electrodes. When apply lower current density of 50, 100, 200 and 400 mA g^{-1}, the SnS/C NFs-650 °C electrode show high discharge capacity of 892, 786, 623 and 475 mA h g^{-1}, respectively. And even at an ultra-high current density of 4000 mA g^{-1}, the discharge capacity of SnS/C NFs-650 °C electrode still can reach to 206 mA h g^{-1} (96 mA h g^{-1} for SnS/C NFs-750 °C; 27 mA h g^{-1} for SnS/C NFs-550 °C). The low capacity of SnS/C NFs-750 °C is attributable to the low SnS content, which is merely 49.4% as mentioned in Section 3.1. For the SnS/C NFs-550 °C, the poor rate performance is on account of the low electrical conductivity by incomplete carbonization of PVP. Fig. S7 displays the digital images of electrode with different calcination stages and different carbonization temperatures. Obviously, the SnS/C NFs with carbonization temperature of 550 °C (Fig. S7d) appear to be in black brown color, which is similar to the samples of before carbonization (Fig. S7b, c). However, the SnS/C NFs with carbonization temperature of 650 °C (Fig. S7e) and 750 °C (Fig. S7f) appear to be consistent black. Further, the conductivity of the SnS/C NFs films with different carbonization temperatures were tested by a four-probe method. The test results of the three films under different test pressures are shown in Table S2. SnS/C NFs-550 °C shows lower conductivity of 5.65E + 03, 5.92E + 03 and 6.21E + 03 S m^{-1} at 1, 2 and 3 MPa, respectively. When the carbonization temperature was raised to 650 °C, the conductivity of the sample increased significantly (2.33E + 04 S m^{-1} at 1 MPa, 2.51E +

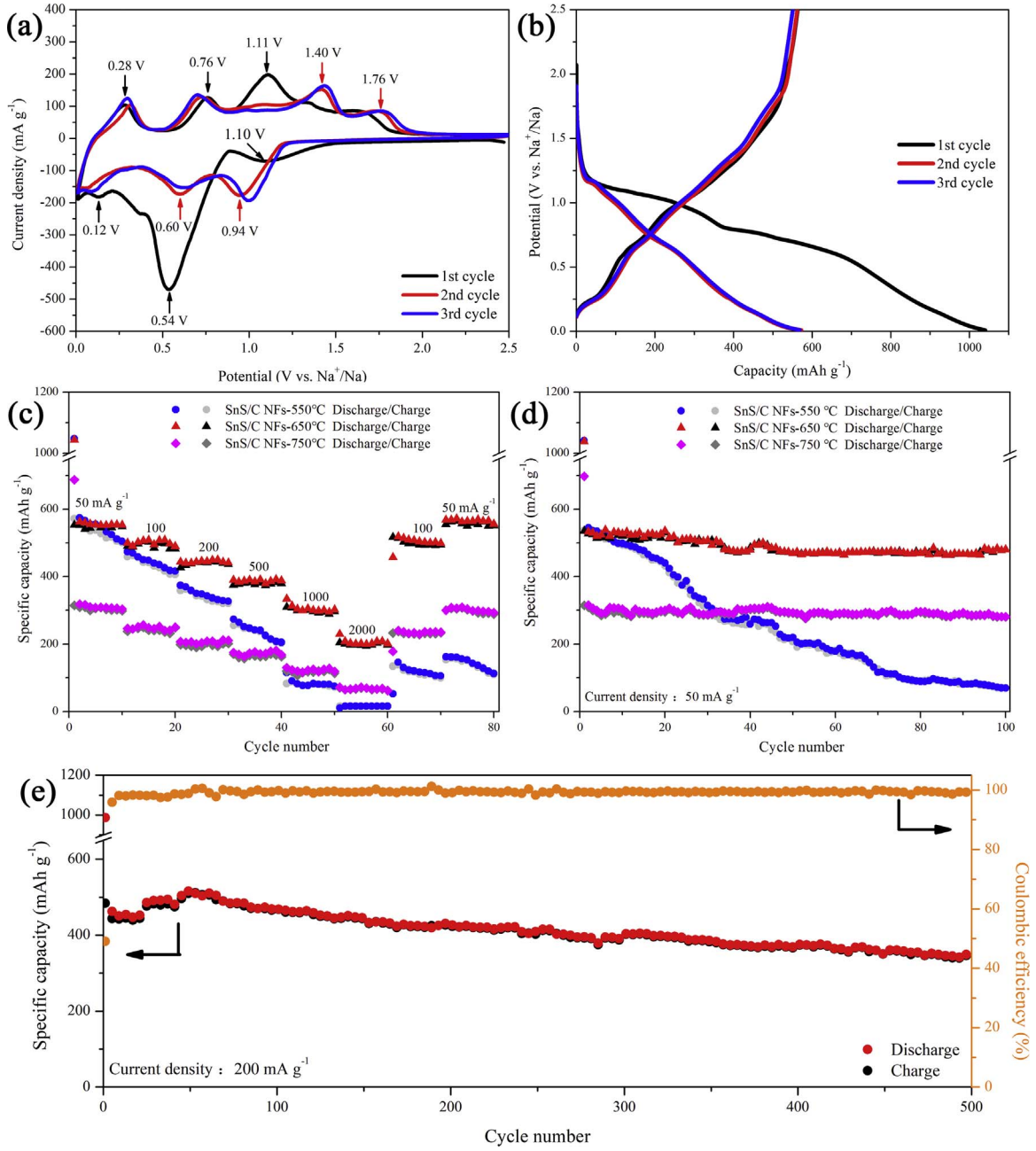

Fig. 7. (a) Cyclic voltammetry curves of SnS/C NFs-650 °C between 0.01 and 2.5 V with a scan rate of 0.1 mV s^{-1}. (b) Discharge-charge voltage profiles of SnS/C NFs-650 °C at a rate of 50 mA g^{-1}. (c) Rate performance of SnS/C NFs with different carbonization temperatures at various current densities from 50 mA g^{-1} to 2000 mA g^{-1}. (d) Cycling performance of SnS/C NFs with different carbonization temperatures at a current density of 50 mA g^{-1}. (e) Long-term cycling performance for SnS/C NFs-650 °C.

04 S m^{-1} at 2 MPa, 2.68E + 04 S m^{-1} at 3 MPa). Further increasing the carbonization temperature to 750 °C, the conductivity still has a small increase. The test results are consistent with the color difference results of SnS/C NFs films with different carbonization temperatures. Obviously, almost full carbonization of PVP is a strong guarantee for good electrical conductivity and excellent rate performance.

Fig. 6d shows the cycling performance of the SnS/C NFs-550 °C, SnS/C NFs-650 °C and SnS/C NFs-750 °C electrodes at 500 mA g^{-1} for 500 cycles. As can be seen, SnS/C NFs-650 °C still delivers an impressively higher capacity of 548 mA h g^{-1} after 500 cycles (170 mA h g^{-1} for SnS/C NFs-750 °C after 500 cycles; 113 mA h g^{-1} for SnS/C NFs-550 °C after 100 cycles). It is noteworthy that the SnS/C NFs-650 °C electrode endured a process of decay and following increasing in capacity. What is known is that the lower carbonization temperature leads to more surface defects on the carbon that allow more lithium ion to store [46]. However, the lower carbonization temperature results in less sintering and less mechanical connection between the fibers, which ultimately leads to sluggish electrical conductivity and poor electrochemical performance. Besides, the large volume change of alloying/de-alloying reaction can cause the SnS particles to pulverized into smaller particles. Smaller particles not only increase the contact area between SnS and the electrolyte, but also provide more accommodation for lithium ion. On the whole, there are three factors that determine the lithium storage capacity of SnS/C NFs: (1) concentration of surface defects; (2) electrical conductivity; (3) content of SnS. Therefore, this is why the SnS/C NFs-650 °C rise to the highest capacity and there is a capacity increase phenomenon because it reaches the best compromise among these three factors. The capacity decay at first 80 cycles could mainly be attributed to the low reversibility of the conversion reaction ($SnS + 2Li^+ + 2e^- \rightarrow Sn + Li_2S$) [47,48]. Fig. S8 compares the CVs of SnS/C NFs with different carbonation temperatures. All samples show similar oxidation/reduction peaks. The SnS/C NFs-650 °C clearly illuminates its high capacity characteristics by the vast integrated area of the CV curve.

To further explain why different carbonization temperatures can cause such large differences in electrochemical performance, electrochemical impedance spectroscopy (EIS) tests of samples with different carbonization temperatures were carried out and compared. As shown in Fig. S9, every Nyquist plot contains a semicircle in the high-frequency region that corresponds to the charge-transfer resistance (R_{ct}), and a sloping line in the low-frequency region represents the diffusion process of ions between the electrode and electrolyte [49]. Nyquist plots are simulated by an equivalent circuit (inset in Fig. S9), and the results are shown in Table S3. The ohm resistance (Rs) shows a small value in all samples with different carbonization temperatures. However, the R_{ct} values show significant differences at different carbonization temperatures, especially the SnS/C NFs-550 °C, its R_{ct} value is even as high as 897 Ω. Poor electrical conductivity is responsible for large R_{ct} values, which seriously hinder charge transfer. When the carbonization temperature rises to 650 °C, the R_{ct} value of the sample drops significantly to 564 Ω. Due to the high carbon content and high graphitization of SnS/C NFs-750 °C, its R_{ct} value is further reduced to 405 Ω. The impedance test results are in good agreement with the above-mentioned Li storage performance.

Furthermore, the SnS/C NFs-650 °C demonstrate ultra-long cycling stability when cycled at 200 mA g^{-1} and 800 mA g^{-1} (Fig. 6e). The SnS/C NFs-650 °C electrode maintained an overall discharge capacity of 648 mA h g^{-1} after 500 discharge/charge cycles at 200 mA g^{-1}. Further investigations were conducted into the cycling performance at 800 mA g^{-1} after 500 cycles at 200 mA g^{-1}. When further increasing the current density to 800 mA g^{-1}, there was a sharp decay in capacity, but the capacity was maintained at a level of 330 mA h g^{-1} after 1000 cycles. To the best of our knowledge, this is the first time such a long cycling life span of SnS material is reported for Li-storage. In addition, the coulombic efficiency also quickly increases to around 99% after the first few discharge/charge cycles. The comparison of the electrochemical performance of SnS/C NFs anode with previously reported SnS-based anodes are listed in Table S4 [4,15,47,50–52]. Clearly, mixing SnS with carbon matrix is a common strategy to improve the electrochemical performance of SnS. However, because of the potential for carbon hasn't been fully excavated, many reported SnS-based composites such as SnS/N-Doped RGO [15], N-doped graphene/SnS [50], SnS/grapheme [51] and SnS nanosheets/RGO [52] show their unsatisfactory electrochemical performance, which is hard to exceed 200 cycles even at a lower current density. The SnS/polypyrrole [4] and the 3D interconnected spherical graphene framework-decorated SnS [47] could delivers considerable reversible capacity of 703 and 527 mA h g^{-1} at 1000 mA g^{-1}, respectively. Regrettably, it is still a rare case to endure over 500 cycles. Additionally, all of these listed electrodes are supported by heavy metal foils with 10–20% non-conducting binders. We prepared the SnS/C NFs films which were directly used as free-standing electrode without the use of metal foils and binders which significantly reduced the weight of electrodes and cost of the cells. Thus, the SnS/C NFs film clearly demonstrated its superiority compared with other listed SnS-based materials.

3.3. Electrochemical evaluation in SIBs

The SnS/C NFs anode also demonstrated excellent electrochemical performance in SIBs. Fig. 7a shows the first three cycles CV for the SnS/C NFs-650 °C anode at the potential window of 0.01 to 2.5 V (vs. Na^+/Na) with the scan rate of 0.1 mV s^{-1}. During the first reduction scan, the peak at 1.10 V is correspond to the conversion reaction of SnS ($SnS + 2Na^+ + 2e^- \leftrightarrow Sn + Na_2S$) [9]. According to previous literatures [53,54], the alloying reaction of Sn and Na commonly occurs at a lower potential of below 0.80 V. Thus, the legible reduction peak at around 0.54 V probably originated from the formation of Na_xSn ($Sn + xNa^+ + xe^- \leftrightarrow Na_xSn$) and SEI film [16]. Another alloying reaction peak located at 0.12 V, revealing a step-by-step alloying process [9,55]. In the reverse anodic scan, the oxidation peaks at 0.28 V and 0.76 V could be attributed to step-by-step dealloying reaction from Na_xSn to Sn [56], and the third oxidation peak at 1.11 V is arises from the back-conversion from Sn and Na_2S to the SnS phase. The shoulder at 1.76 V may be related to a reaction between S and Na in the –C–S–C– bond of carbon matrix [13,57]. There is such an obvious difference between the first scan and subsequent scans, which is mainly attributed to the inevitable formation of SEI film and an activation process of electrode. Besides, three pairs of oxidation/reduction peaks located at 0.28/0.12 V, 0.76/0.60 V, and 1.40/0.94 V for subsequent cycles are still apparent, indicating a good reversibility for the SnS/C NFs electrode. Fig. 7b shows the galvanostatic discharge-charge curves of the SnS/C NFs-650 °C anode at a rate of 50 mA g^{-1} for the first three cycles. Alike LIBs, the first discharge capacity loss in SIBs is also mainly attributed to the irreversible formation of SEI films and the electrolyte decomposition. From the second cycle onward, almost overlapping discharge-charge curves are observed, mean that outstanding cycling stability and minimal polarization for SnS/C NFs anode.

The rate performance of SnS/C NFs anode with different carbonization temperatures for SIBs at various current densities from 50 mA g^{-1} to 2000 mA g^{-1} is displayed in Fig. 7c. As with the lithium storage performance, SnS/C NFs-650 °C electrode shows best rate performance compared with other two electrodes. When the current density gradually increasing (50, 100, 200, 500, 1000 and 2000 mA g^{-1}), the SnS/C NFs-650 °C electrode delivered discharge capacities were 563, 500, 444, 390, 334 and 230 mA h g^{-1}, correspondingly. Further, when the current density is reset to 100 and 50 mA g^{-1}, the discharge and charge capacity can fully recover, which is crucial for the applications of high power sodium ion battery.

Fig. 7d shows the cycle life of three electrode at 50 mA g^{-1} in SIBs. After 100 cycles, the SnS/C NFs-650 °C electrode still maintains discharge capacity of 481 mA h g^{-1} with a capacity retention rate of 90.2%. In comparison, the control sample SnS/C NFs-750 °C shows

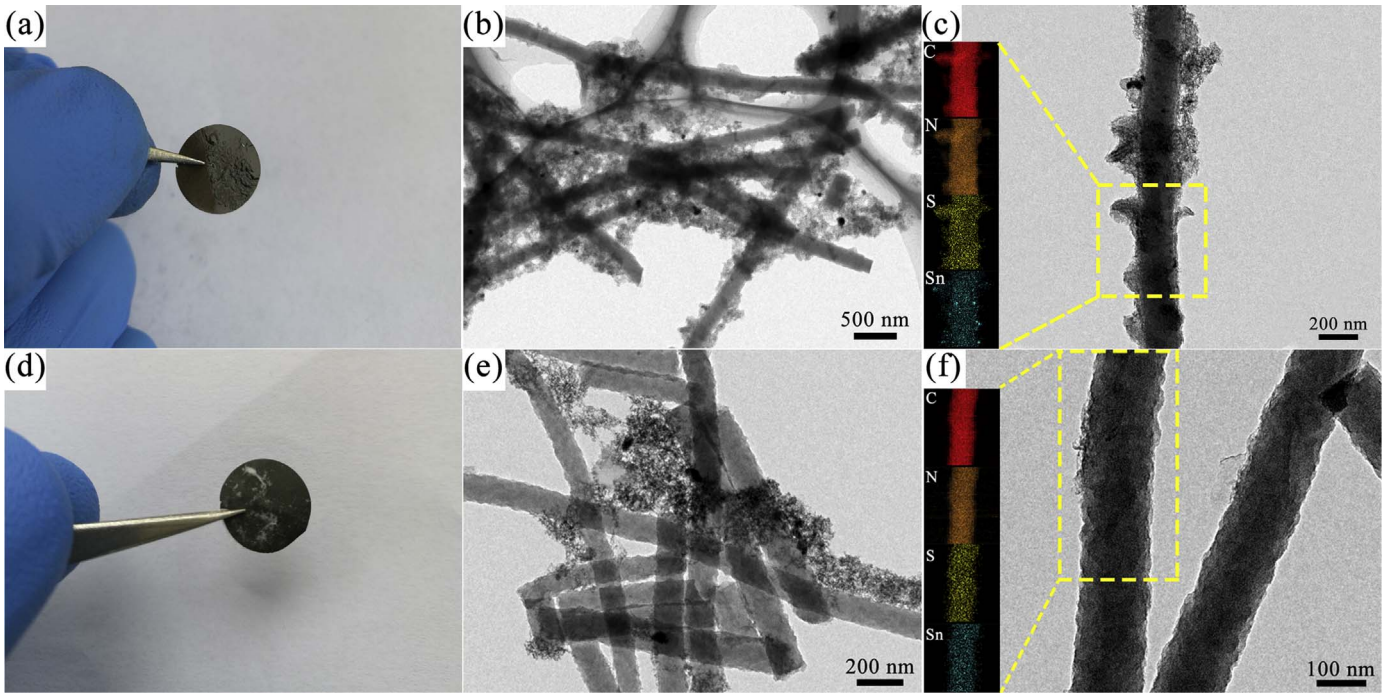

Fig. 8. Digital (a) and TEM (b, c) images of the SnS/C NFs-650 °C electrode after cycling for 500 cycles at 500 mA g^{-1} in LIBs (the EDX elemental mapping of the area, marked by the yellow rectangle in image c). Digital (d) and TEM (e, f) images of the SnS/C NFs-650 °C electrode after cycling for 100 cycles at 50 mA g^{-1} in SIBs (the EDX elemental mapping of the area, marked by the yellow rectangle in image f). (For interpretation of the references to color in this figure legend, the reader is referred to the web version of this article.)

similar cycle stability, but this sample delivers a discharge capacity of merely 281 mA h g^{-1}. The low capacity is attributable to the low SnS content, which is mentioned in the above description. The capacity of SnS/C NFs-550 °C is terribly dropped to only 70 mA h g^{-1} after 100 cycles that is worst, owing to low electronic conductivity. The comparison of CV curves in Fig. S10 also illustrates that SnS/C NFs-650 °C has good reversibility and the highest capacity compared to SnS/C NFs-550 °C and SnS/C NFs-750 °C. In addition, the Nyquist plots (Fig. S11) of the SnS/C NFs with different carbonation temperatures in SIBs also show similar characteristics to LIBs. The simulated results are shown in Table S5. The R_{ct} value of SnS/C NFs-550 °C sample is as high as 1545 Ω, which also caused its terrible Na storage performance. Compared to SnS/C NFs-550 °C, the R_{ct} values of SnS/C NFs-650 °C and SnS/C NFs-750 °C are much smaller. Therefore, good cycle stability and rate performance are obtained for SnS/C NFs-650 °C and SnS/C NFs-750 °C. Nevertheless, it is important to note that the R_{ct} value of SnS/C NFs is much larger in SIBs than in LIBs at the same carbonization temperature. The larger impedance values in SIBs are mainly attributed to the large sodium ion radius leading to the sluggish sodium ion diffusion kinetics.

In order to further evaluate the long-term cycle stability of the SnS/C NFs-650 °C electrode, a higher current density of 200 mA g^{-1} was conducted to execute the galvanostatic discharge-charge measurement, and the result is shown in Fig. 7e. After 500 cycles, the SnS/C NFs-650 °C electrode can still deliver a capacity of 349 mA h g^{-1}. The sodium storage performance of SnS/C NFs-650 °C electrode in terms of cycling stability are superior to that of many SnS-based anodes reported in literature (Table S6) [13,14,58–61]. Normally, larger sized Na^+ leads to sluggish Na^+ diffusion rate and greater volumetric change, ultimately leads to poor electrochemical performance, which means that the unmodified SnS is difficult to apply in SIBs. For example, Mitra's group [58] reported the sodium storage performance of bare SnS, sure enough, its capacity is only 370 mA h g^{-1} after 30 cycles cycling at 125 mA g^{-1}. Similar to LIBs, in order to improve the electrochemical performance of SIBs, lots of research efforts are devoted to mixing SnS with carbon matrix such as multi walled carbon nanotube (MWCNT), graphene and other carbon materials. Such as Kang's group [59], Li's group [60] and Cao's group [61] have gained great success in performance improvement of SnS by the addition of carbonaceous materials. Especially the Guo's group [14] reported the SnS/graphene, its reversible capacity could be improved to 308 mA h g^{-1} after 250 cycles at 7290 mA g^{-1}. More strikingly, Yu's group [13] have prepared the carbon-coated SnS by the SnS/C nanocomposites deposited on the Ti current collector and directly used as working electrode without the use of binder. When evaluated as anode material for SIBs, this composite could deliver reversible discharge capacity of 266 mA h g^{-1} after 300 cycles. Regrettably, this composite still requires a heavy Ti current collector as a support, not only difficult to achieve the application of flexible electronics and wearable devices, but also increase the cost of the cell. Moreover, all of these SnS-based electrodes quoted in Table S3 are inflexible and few cases can endure over 300 cycles. These fully demonstrate the SnS/C NFs prepared by electrospinning is a promising anode material for wearable electronics applications.

3.4. Characterization of after-cycled SnS/C NFs electrode for LIBs and SIBs

To investigate the mechanism for the excellent cycling stability of SnS/C NFs electrode, the lithium cell tested at 500 mA g^{-1} rate for 500 cycles as well as the sodium cell tested at 50 mA g^{-1} rate for 100 cycles was disassembled, and the micromorphology of the SnS/C NFs electrodes were studied using TEM. Before taking the images, the after-cycled electrodes were rinsed with dimethyl carbonate (DMC) to remove the electrolyte residue on the fibers. Fig. 8a and d show the digital images of after-cycled electrode in LIBs and SIBs, respectively. As can be seen, the after-cycled SnS/C NFs electrode still maintained its structural integrity and flexibility both in LIBs and SIBs. It should be noted that a small amount of white floc can be observed on sodium-ion battery electrode which is from the glass fiber film. The TEM images in Fig. 8b and e show that an SEI film covered the SnS/C NFs. The SEI film is mainly formed in the first cycle, which might be the reason accounting for the low initial coulombic efficiency. Moreover, the diameter of the fibers was uniform (Fig. 8b, e) and similar to that of

the uncycled fibers (Fig. 5a), suggesting that this electrode structure can effectively accommodate the volume change during cycling. Besides, as shown by the TEM images of after-cycled fiber and its EDX element mapping (Fig. 8c and f), after a sustainable number of cycles, the C, N, S and Sn element still uniformly distributed in the nanofibers, indicating the mechanical stability of the fibers. It is to be observed that the after-cycled fiber surface is smoother in SIBs than in LIBs, which is mainly due to the addition of FEC in the SIBs electrolyte. As is well known, the SEI films formed on the electrodes are fragile and easily damaged during repeated cycling, causing the continuous creation of new SEI films [62,63]. Therefore, the thick and rough SEI films in LIBs mainly due to the damage of the fragile SEI films and the continuous accumulation of fresh SEI films. FEC can facilitate the formation of compact SEI film consisting mainly of stable fluroalkyl carbonate or alkali fluoride on the electrodes, and is considered an effective electrolyte additive for improvement of SEI films [63]. So the compact SEI film could formed on the electrodes in SIBs.

4. Conclusions

Achieving excellent electrochemical performance while maintaining the robust flexibility of electrode in LIBs and SIBs is vital to develop flexible electronics and wearable devices. In this study, a novel SnS/C nanofibers film was firstly synthesized by electrospinning and subsequent calcination. The nanofibers are closely woven into interconnecting network, not only can endure 30 g weight without breakage, but also can recover its initial state after being folded, bent and kneaded one by one, indicating that this nanofiber film has ultra-robust flexibility. When this nanofiber film is directly used in LIBs and SIBs as a free-standing electrode, it shows outstanding electrochemical performance. In particular, the sample with the calcining temperature of 650 °C (that is SnS/C NFs-650 °C) achieved the best compromise (compared to 550 °C and 750 °C) among the three factors of concentration of surface defects, electrical conductivity and content of SnS, thereby obtaining the best electrochemical performance including high reversible capacity, ultralong cycling life span and excellent rate capability as free-standing electrodes for both LIBs and SIBs. Further, the outstanding electrochemical performance of SnS/C NFs-650 °C is also originated from following four points. Firstly, fine 1D porous nanostructure with uniform diameters around 130 nm can shorten the transport path of Li^+, Na^+ and electron. Secondly, the fine SnS with the diameter of 1–3 nm dispersed in the carbon fibers, can better relieve the volume change caused by the alloying/de-alloying reaction. Thirdly, self-doped N contributed a large number of electrons for SnS/C NFs, which improves the electronic conductivity of the composites. Lastly, its most remarkable to find that the after-cycled SnS/C NFs-650 °C electrode still maintained its structural integrity and flexibility both in LIBs and SIBs , which is an important guarantee for long-term cycle stability. These merits ensure that SnS/C NFs electrodes are promising candidates for flexible lithium/sodium ion battery anode.

Acknowledgments

This work was supported financially by the National Natural Science Foundation of China (Grant No. 51672234), the Research Foundation for Hunan Youth Outstanding People from Hunan Provincial Science and Technology Department (2015RS4030), Hunan 2011 Collaborative Innovation Center of Chemical Engineering & Technology with Environmental Benignity and Effective Resource Utilization, Program for Innovative Research Cultivation Team in University of Ministry of Education of China (1337304), and the 111 Project (B12015).

Appendix A. Supplementary material

Supplementary data associated with this article can be found in the online version at doi:10.1016/j.ensm.2018.08.005.

References

[1] S. Peng, L. Li, J. Kong Yoong Lee, L. Tian, M. Srinivasan, S. Adams, S. Ramakrishna, Electrospun carbon nanofibers and their hybrid composites as advanced materials for energy conversion and storage, Nano Energy 22 (2016) 361–395. http://dx.doi.org/10.1016/j.nanoen.2016.02.001.
[2] N. Armaroli, V. Balzani, The future of energy supply: challenges and opportunities, Angew. Chem. Int. Ed. 46 (2007) 52–66. http://dx.doi.org/10.1002/anie.200602373.
[3] Y. Liu, N. Zhang, L. Jiao, Z. Tao, J. Chen, Ultrasmall Sn Nanoparticles Embedded in Carbon as High- Performance Anode for Sodium-Ion Batteries, 2015, pp. 214–220. ⟨https://dx.doi.org/10.1002/adfm.201402943⟩.
[4] J. Liu, M. Gu, L. Ouyang, H. Wang, L. Yang, M. Zhu, Sandwich-like SnS/polypyrrole ultrathin nanosheets as high-performance anode materials for Li-ion batteries, ACS Appl. Mater. Interfaces 8 (2016) 8502–8510. http://dx.doi.org/10.1021/acsami.6b00627.
[5] M. Mao, C. Cui, M. Wu, M. Zhang, T. Gao, X. Fan, J. Chen, T. Wang, J. Ma, C. Wang, Flexible ReS_2 nanosheets/N-doped carbon nanofibers-based paper as a universal anode for alkali (Li, Na, K) ion battery, Nano Energy 45 (2018) 346–352. http://dx.doi.org/10.1016/j.nanoen.2018.01.001.
[6] B. Qu, C. Ma, G. Ji, C. Xu, J. Xu, Y.S. Meng, T. Wang, J.Y. Lee, Layered SnS_2-reduced graphene oxide composite - A high-capacity, high-rate, and long-cycle life sodium-ion battery anode material, Adv. Mater. 26 (2014) 3854–3859. http://dx.doi.org/10.1002/adma.201306314.
[7] J.W. Seo, J.T. Jang, S.W. Park, C. Kim, B. Park, J. Cheon, Two-dimensional SnS2nanoplates with extraordinary high discharge capacity for lithium ion batteries, Adv. Mater. 20 (2008) 4269–4273. http://dx.doi.org/10.1002/adma.200703122.
[8] J. Xia, L. Liu, J. Xie, H. Yan, Y. Yuan, M. Chen, C. Huang, Y. Zhang, S. Nie, X. Wang, Layer-by-layered SnS_2/graphene hybrid nanosheets via ball-milling as promising anode materials for lithium ion batteries, Electrochim. Acta 269 (2018) 452–461. http://dx.doi.org/10.1016/j.electacta.2018.03.022.
[9] X. Xiong, C. Yang, G. Wang, Y. Lin, X. Ou, J.-H. Wang, B. Zhao, M. Liu, Z. Lin, K. Huang, SnS nanoparticles electrostatically anchored on three-dimensional N-doped graphene as an active and durable anode for sodium-ion batteries, Energy Environ. Sci. 10 (2017) 1757–1763. http://dx.doi.org/10.1039/C7EE01628J.
[10] Q. Zhou, L. Liu, Z. Huang, L. Yi, X. Wang, G. Cao, Co_3S_4@polyaniline nanotubes as high-performance anode materials for sodium ion batteries, J. Mater. Chem. A 4 (2016) 5505–5516. http://dx.doi.org/10.1039/C6TA01497F.
[11] J. Xie, L. Liu, J. Xia, Y. Zhang, M. Li, Y. Ouyang, S. Nie, X. Wang, Template-free synthesis of Sb_2S_3 hollow microspheres as anode materials for lithium-ion and sodium-ion batteries, Nano-Micro Lett. 10 (2018) 12. http://dx.doi.org/10.1007/s40820-017-0165-1.
[12] L. Wang, Q. Zhang, J. Zhu, X. Duan, Z. Xu, Y. Liu, Nature of Extra Capacity in MoS_2 Electrodes : Molybdenum Atoms Accommodate with Lithium, 16, 2019, pp. 37–45. ⟨https://dx.doi.org/10.1016/j.ensm.2018.04.025⟩.
[13] C. Zhu, P. Kopold, W. Li, P.A. van Aken, J. Maier, Y. Yu, A general strategy to fabricate carbon-coated 3D porous interconnected metal sulfides: case study of SnS/C nanocomposite for high-performance lithium and sodium ion batteries, Adv. Sci. 2 (2015) 1–8. http://dx.doi.org/10.1002/advs.201500200.
[14] T. Zhou, W.K. Pang, C. Zhang, J. Yang, Z. Chen, H.K. Liu, Z. Guo, Enhanced sodium-ion battery performance by structural phase transition from two-dimensional hexagonal-SnS_2 to orthorhombic-SnS, ACS Nano 8 (2014) 8323–8333. http://dx.doi.org/10.1021/nn503582c.
[15] D.H. Youn, S.K. Stauffer, P. Xiao, H. Park, Y. Nam, A. Dolocan, G. Henkelman, A. Heller, C.B. Mullins, Simple synthesis of nanocrystalline tin sulfide/N-doped reduced graphene oxide composites as lithium ion battery anodes, ACS Nano 10 (2016) 10778–10788. http://dx.doi.org/10.1021/acsnano.6b04214.
[16] L. Wu, H. Lu, L. Xiao, J. Qian, X. Ai, H. Yang, Y. Cao, A tin(ii) sulfide-carbon anode material based on combined conversion and alloying reactions for sodium-ion batteries, J. Mater. Chem. A 2 (2014) 16424–16428. http://dx.doi.org/10.1039/C4TA03365E.
[17] J. Sheng, L. Yang, Y.-E. Zhu, F. Li, Y. Zhang, Z. Zhou, Oriented SnS nanoflakes bound on S-doped N-rich carbon nanosheets with a rapid pseudocapacitive response as high-rate anodes for sodium-ion batteries, J. Mater. Chem. A 5 (2017) 19745–19751. http://dx.doi.org/10.1039/C7TA06577A.
[18] V. Thavasi, G. Singh, S. Ramakrishna, Electrospun nanofibers in energy and environmental applications, Energy Environ. Sci. 1 (2008) 205–221. http://dx.doi.org/10.1039/B809074M.
[19] S. Peng, G. Jin, L. Li, K. Li, M. Srinivasan, S. Ramakrishna, J. Chen, Multi-functional electrospun nanofibres for advances in tissue regeneration, energy conversion & storage, and water treatment, Chem. Soc. Rev. 45 (2016) 1225–1241. http://dx.doi.org/10.1039/C5CS00777A.
[20] W. Li, L. Zeng, Y. Wu, Y. Yu, Nanostructured electrode materials for lithium-ion and sodium-ion batteries via electrospinning, Sci. China Mater. 59 (2016) 287–321. http://dx.doi.org/10.1007/s40843-016-5039-6.
[21] T. Jin, Q. Han, Y. Wang, L. Jiao, 1D Nanomaterials: Design, Synthesis, and Applications in Sodium–Ion Batteries, 1703086, 2018, pp. 1–26. ⟨https://dx.doi.org/10.1002/smll.201703086⟩.

[22] J. Madarász, G. Pokol, Comparative evolved gas analyses on thermal degradation of thiourea by coupled TG-FTIR and TG/DTA-MS instruments, J. Therm. Anal. Calorim. 88 (2007) 329–336. http://dx.doi.org/10.1007/s10973-006-8058-4.
[23] S. Notes, A.W. Parke, G.P. Sfuvastava, The Electronic Band Structure of SnS, 31, 1980, pp. 7–11.
[24] N.K. Reddy, Growth-temperature dependent physical properties of SnS nanocrystalline thin films, ECS J. Solid State Sci. Technol. 2 (2013) P259–P263. http://dx.doi.org/10.1149/2.006306jss.
[25] P.A. Nwofe, K.T.R. Reddy, G. Sreedevi, J.K. Tan, I. Forbes, R.W. Miles, Single phase, large grain, p-conductivity-type SnS layers produced using the thermal evaporation method, Energy Procedia 15 (2012) 354–360. http://dx.doi.org/10.1016/j.egypro.2012.02.043.
[26] A.C. Ferrari, J.C. Meyer, V. Scardaci, C. Casiraghi, M. Lazzeri, F. Mauri, S. Piscanec, D. Jiang, K.S. Novoselov, S. Roth, A.K. Geim, Raman spectrum of graphene and graphene layers, Phys. Rev. Lett. 97 (2006) 1–4. http://dx.doi.org/10.1103/PhysRevLett.97.187401.
[27] Z. Liu, X.-Y. Yu, X.W. (David) Lou, U. Paik, Sb@C coaxial nanotubes as a superior long-life and high-rate anode for sodium ion batteries, Energy Environ. Sci. 9 (2016) 2314–2318. http://dx.doi.org/10.1039/C6EE01501H.
[28] D. Xiong, Q. Zhang, W. Li, J. Li, X. Fu, M.F. Cerqueira, P. Alpuim, L. Liu, Atomic-layer-deposited ultrafine MoS_2 nanocrystals on cobalt foam for efficient and stable electrochemical oxygen evolution, Nanoscale 9 (2017) 2711–2717. http://dx.doi.org/10.1039/C7NR00140A.
[29] Z. Wang, Y. Dong, H. Li, Z. Zhao, H. Bin Wu, C. Hao, S. Liu, J. Qiu, X.W.D. Lou, Enhancing lithium-sulphur battery performance by strongly binding the discharge products on amino-functionalized reduced graphene oxide, Nat. Commun. 5 (2014) 1–8. http://dx.doi.org/10.1038/ncomms6002.
[30] Y. Yan, Y.-X. Yin, S. Xin, Y.-G. Guo, L.-J. Wan, Ionothermal synthesis of sulfur-doped porous carbons hybridized with graphene as superior anode materials for lithium-ion batteries, Chem. Commun. 48 (2012) 10663–10665. http://dx.doi.org/10.1039/C2CC36234A.
[31] X. Ma, G. Ning, Y. Kan, Y. Ma, C. Qi, B. Chen, Y. Li, X. Lan, J. Gao, Synthesis of S-doped mesoporous carbon fibres with ultrahigh S concentration and their application as high performance electrodes in supercapacitors, Electrochim. Acta 150 (2014) 108–113. http://dx.doi.org/10.1016/j.electacta.2014.10.128.
[32] W. Li, M. Zhou, H. Li, K. Wang, S. Cheng, K. Jiang, A high performance sulfur-doped disordered carbon anode for sodium ion batteries, Energy Environ. Sci. 8 (2015) 2916–2921. http://dx.doi.org/10.1039/C5EE01985K.
[33] H. Wang, K. Dou, W.Y. Teoh, Y. Zhan, T.F. Hung, F. Zhang, J. Xu, R. Zhang, A.L. Rogach, Engineering of facets, band structure, and gas-sensing properties of hierarchical Sn^{2+}-doped SnO_2 nanostructures, Adv. Funct. Mater. 23 (2013) 4847–4853. http://dx.doi.org/10.1002/adfm.201300303.
[34] D. Chen, G. Shen, K. Tang, S. Lei, H. Zheng, Y. Qian, Microwave-assisted polyol synthesis of nanoscale SnS_x(x = 1, 2) flakes, J. Cryst. Growth 260 (2004) 469–474. http://dx.doi.org/10.1016/j.jcrysgro.2003.09.009.
[35] J.M. Burkstrand, Copper-polyvinyl alcohol interface: a study with XPS, J. Vac. Sci. Technol. 16 (1979) 363–365. http://dx.doi.org/10.1116/1.569951.
[36] E. Unger, A. Graham, F. Kreupl, M. Liebau, W. Hoenlein, Electrochemical functionalization of multi-walled carbon nanotubes for solvation and purification, Curr. Appl. Phys. 2 (2002) 107–111. http://dx.doi.org/10.1016/S1567-1739(01)00072-4.
[37] H. Bai, Y. Xu, L. Zhao, C. Li, G. Shi, Non-covalent functionalization of graphene sheets by sulfonated polyaniline, Chem. Commun. (2009) 1667–1669. http://dx.doi.org/10.1039/B821805F.
[38] D.P. Dubal, N.R. Chodankar, Z. Caban-Huertas, F. Wolfart, M. Vidotti, R. Holze, C.D. Lokhande, P. Gomez-Romero, Synthetic approach from polypyrrole nanotubes to nitrogen doped pyrolyzed carbon nanotubes for asymmetric supercapacitors, J. Power Sources 308 (2016) 158–165. http://dx.doi.org/10.1016/j.jpowsour.2016.01.074.
[39] Y. Liu, N. Zhang, L. Jiao, J. Chen, Tin nanodots encapsulated in porous nitrogen-doped carbon nanofibers as a free-standing anode for advanced sodium-ion batteries, Adv. Mater. 27 (2015) 6702–6707. http://dx.doi.org/10.1002/adma.201503015.
[40] Z. Zhu, S. Wang, J. Du, Q. Jin, T. Zhang, F. Cheng, J. Chen, Ultrasmall Sn nanoparticles embedded in nitrogen-doped porous carbon as high-performance anode for lithium-ion batteries, Nano Lett. 14 (2014) 153–157. http://dx.doi.org/10.1021/nl403631h.
[41] W. Shen, C. Wang, Q. Xu, H. Liu, Y. Wang, Nitrogen-doping-induced defects of a carbon coating layer facilitate Na-storage in electrode materials, Adv. Energy Mater. 5 (2015). http://dx.doi.org/10.1002/aenm.201400982.
[42] J. Cai, Z. Li, P.K. Shen, Porous SnS nanorods/carbon hybrid materials as highly stable and high capacity anode for Li-ion batteries, ACS Appl. Mater. Interfaces 4 (2012) 4093–4098. http://dx.doi.org/10.1021/am300873n.
[43] J. Lu, C. Nan, L. Li, Q. Peng, Y. Li, Flexible SnS nanobelts: facile synthesis, formation mechanism and application in Li-ion batteries, Nano Res. 6 (2013) 55–64. http://dx.doi.org/10.1007/s12274-012-0281-7.
[44] Z. Deng, H. Jiang, Y. Hu, C. Li, Y. Liu, H. Liu, Nanospace-confined synthesis of coconut-like SnS/C nanospheres for high-rate and stable lithium-ion batteries, AIChE J. 0 (2018) 1–10. http://dx.doi.org/10.1002/aic.16068.
[45] W. Ai, Z. Huang, L. Wu, Z. Du, C. Zou, Z. He, High-rate, long cycle-life Li-ion battery anodes enabled by ultrasmall tin-based nanoparticles encapsulation, Energy Storage Mater. 14 (2018) 169–178. http://dx.doi.org/10.1016/j.ensm.2018.02.008.
[46] L. Wang, Y. Yu, P.C. Chen, D.W. Zhang, C.H. Chen, Electrospinning synthesis of C/Fe_3O_4 composite nanofibers and their application for high performance lithium-ion batteries, J. Power Sources 183 (2008) 717–723. http://dx.doi.org/10.1016/j.jpowsour.2008.05.079.
[47] B. Zhao, Z. Wang, F. Chen, Y. Yang, Y. Gao, L. Chen, Z. Jiao, L. Cheng, Y. Jiang, Three-dimensional interconnected spherical graphene framework/SnS nanocomposite for anode material with superior lithium storage performance: complete reversibility of Li_2S, ACS Appl. Mater. Interfaces 9 (2017) 1407–1415. http://dx.doi.org/10.1021/acsami.6b10708.
[48] X.L. Gou, J. Chen, P.W. Shen, Synthesis, characterization and application of SnS_x(x = 1, 2) nanoparticles, Mater. Chem. Phys. 93 (2005) 557–566. http://dx.doi.org/10.1016/j.matchemphys.2005.04.008.
[49] J. Xie, Y. Pei, L. Liu, S. Guo, J. Xia, M. Li, Y. Ouyang, X. Zhang, X. Wang, Hydrothermal synthesis of antimony oxychlorides submicron rods as anode materials for lithium-ion batteries and sodium-ion batteries, Electrochim. Acta. 254 (2017) 246–254. http://dx.doi.org/10.1016/j.electacta.2017.09.136.
[50] S.C. Zhu, H.C. Tao, X.L. Yang, L.L. Zhang, S.B. Ni, Synthesis of N-doped graphene/SnS composite and its electrochemical properties for lithium ion batteries, Ionics 21 (2015) 2735–2742. http://dx.doi.org/10.1007/s11581-015-1490-3.
[51] H.C. Tao, X.L. Yang, L.L. Zhang, S.B. Ni, One-step in situ synthesis of SnS/graphene nanocomposite with enhanced electrochemical performance for lithium ion batteries, J. Electroanal. Chem. 728 (2014) 134–139. http://dx.doi.org/10.1016/j.jelechem.2014.07.004.
[52] S. Li, J. Zheng, S. Zuo, Z. Wu, P. Yan, F. Pan, 2D hybrid anode based on SnS nanosheet bonded with graphene to enhance electrochemical performance for lithium-ion batteries, RSC Adv. 5 (2015) 46941–46946. http://dx.doi.org/10.1039/C5RA07292A.
[53] L. Xiao, Y. Cao, J. Xiao, W. Wang, L. Kovarik, Z. Nie, J. Liu, High capacity, reversible alloying reactions in SnSb/C nanocomposites for Na-ion battery applications, Chem. Commun. 48 (2012) 3321–3323. http://dx.doi.org/10.1039/C2CC17129E.
[54] Z. Li, J. Ding, D. Mitlin, Tin and tin compounds for sodium ion battery anodes: phase transformations and performance, Acc. Chem. Res. 48 (2015) 1657–1665. http://dx.doi.org/10.1021/acs.accounts.5b00114.
[55] J.M. Stratford, M. Mayo, P.K. Allan, O. Pecher, O.J. Borkiewicz, K.M. Wiaderek, K.W. Chapman, C.J. Pickard, A.J. Morris, C.P. Grey, Investigating sodium storage mechanisms in tin anodes: a combined pair distribution function analysis, density functional theory, and solid-state NMR approach, J. Am. Chem. Soc. 139 (2017) 7273–7286. http://dx.doi.org/10.1021/jacs.7b01398.
[56] S. Chen, Z. Ao, B. Sun, X. Xie, G. Wang, Porous carbon nanocages encapsulated with tin nanoparticles for high performance sodium-ion batteries, Energy Storage Mater. 5 (2016) 180–190. http://dx.doi.org/10.1016/j.ensm.2016.07.001.
[57] J. Yang, X. Zhou, D. Wu, X. Zhao, Z. Zhou, S-doped N-rich carbon nanosheets with expanded interlayer distance as anode materials for sodium-ion batteries, Adv. Mater. 29 (2017) 1–5. http://dx.doi.org/10.1002/adma.201604108.
[58] P.K. Dutta, U.K. Sen, S. Mitra, Excellent electrochemical performance of tin monosulphide (SnS) as a sodium-ion battery anode, RSC Adv. 4 (2014) 43155–43159. http://dx.doi.org/10.1039/C4RA05851H.
[59] S.H. Choi, Y.C. Kang, Aerosol-assisted rapid synthesis of SnS-C composite microspheres as anode material for Na-ion batteries, Nano Res. 8 (2015) 1595–1603. http://dx.doi.org/10.1007/s12274-014-0648-z.
[60] W. Wang, L. Shi, D. Lan, Q. Li, Improving cycle stability of SnS anode for sodium-ion batteries by limiting Sn agglomeration, J. Power Sources 377 (2018) 1–6. http://dx.doi.org/10.1016/j.jpowsour.2017.11.084.
[61] L. Wu, H. Lu, L. Xiao, J. Qian, X. Ai, H. Yang, Y. Cao, A tin(ii) sulfide–carbon anode material based on combined conversion and alloying reactions for sodium-ion batteries, J. Mater. Chem. A 2 (2014) 16424–16428. http://dx.doi.org/10.1039/C4TA03365E.
[62] S. Komaba, T. Ishikawa, N. Yabuuchi, W. Murata, A. Ito, Y. Ohsawa, Fluorinated ethylene carbonate as electrolyte additive for rechargeable Na batteries, ACS Appl. Mater. Interfaces 3 (2011) 4165–4168. http://dx.doi.org/10.1021/am200973k.
[63] J. Qian, Y. Chen, L. Wu, Y. Cao, X. Ai, H. Yang, High capacity Na-storage and superior cyclability of nanocomposite Sb/C anode for Na-ion batteries, Chem. Commun. 48 (2012) 7070–7072. http://dx.doi.org/10.1039/C2CC32730A.